A&A 608, A27 (2017)
DOI: 10.1051/0004-6361/201731357

Astronomy & Astrophysics

The spatially resolved star formation history of CALIFA galaxies

Cosmic time scales

R. García-Benito[1], R. M. González Delgado[1], E. Pérez[1], R. Cid Fernandes[2], C. Cortijo-Ferrero[1], R. López Fernández[1], A. L. de Amorim[2], E. A. D. Lacerda[2], N. Vale Asari[2], S. F. Sánchez[3], and the CALIFA team*

[1] Instituto de Astrofísica de Andalucía (CSIC), PO Box 3004, 18080 Granada, Spain
e-mail: rgb@iaa.es
[2] Departamento de Física, Universidade Federal de Santa Catarina, PO Box 476, 88040-900 Florianópolis, SC, Brazil
[3] Instituto de Astronomía, Universidad Nacional Autonóma de México, AP 70-264, 04510 México DF, Mexico

Received 13 June 2017 / Accepted 28 August 2017

ABSTRACT

This paper presents the mass assembly time scales of nearby galaxies observed by CALIFA at the 3.5 m telescope in Calar Alto. We apply the fossil record method of the stellar populations to the complete sample of the 3rd CALIFA data release, with a total of 661 galaxies, covering stellar masses from $10^{8.4}$ to 10^{12} $M_\odot$ and a wide range of Hubble types. We apply spectral synthesis techniques to the datacubes and process the results to produce the mass growth time scales and mass weighted ages, from which we obtain temporal and spatially resolved information in seven bins of galaxy morphology (E, S0, Sa, Sb, Sc, and Sd) and six bins of stellar mass and stellar mass surface density. We use three different tracers of the spatially resolved star formation history (mass assembly curves, ratio of half mass to half light radii, and mass-weighted age gradients) to test if galaxies grow inside-out, and its dependence with galaxy stellar mass, stellar mass surface density, and morphology. Our main results are as follows: (a) the innermost regions of galaxies assemble their mass at an earlier time than regions located in the outer parts; this happens at any given stellar mass ($M_\star$), stellar mass surface density ($\Sigma_\star$), or Hubble type, including the lowest mass systems in our sample. (b) Galaxies present a significant diversity in their characteristic formation epochs for lower-mass systems. This diversity shows a strong dependence of the mass assembly time scales on $\Sigma_\star$ and Hubble type in the lower-mass range ($10^{8.4}$ to $10^{10.4}$), but a very mild dependence in higher-mass bins. (c) The lowest half mass radius (HMR) to half light radius (HLR) ratio is found for galaxies between $10^{10.4}$ and $10^{11.1}$ $M_\odot$, where galaxies are 25% smaller in mass than in light. Low-mass galaxies show the largest ratio with HMR/HLR ~ 0.89. Sb and Sbc galaxies present the lowest HMR/HLR ratio (0.74). The ratio HMR/HLR is always, on average, below 1, indicating that galaxies grow faster in mass than in light. (d) All galaxies show negative $\langle \log \text{age} \rangle_M$ gradients in the inner 1 HLR. The profile flattens (slope less negative) with increasing values of $\Sigma_\star$. There is no significant dependence on $M_\star$ within a particular $\Sigma_\star$ bin, except for the lowest bin, where the gradients becomes steeper. (e) Downsizing is spatially preserved as a function of $M_\star$ and $\Sigma_\star$, but it is broken for E and SO where the outer parts are assembled in later epochs than Sa galaxies. These results suggest that independently of their stellar mass, stellar mass surface density, and morphology, galaxies form inside-out on average.

Key words. techniques: spectroscopic – galaxies: general – galaxies: formation – galaxies: evolution – galaxies: star formation – surveys

1. Introduction

Tracing how galaxies grow their stellar mass as a function of cosmic time is key to understanding how galaxies form and evolve. Nowadays, a two-phase scenario is proposed for the formation of massive galaxies in which ellipticals (E) form first a dense core at high redshift, and subsequently grow their outer envelope (van Dokkum et al. 2010; Patel et al. 2013). This mass growth occurs with a significant increase of their size (Trujillo et al. 2006; Buitrago et al. 2008) that is produced mainly by dry mergers (Naab et al. 2009; Oser et al. 2010; Hilz et al. 2013). As the central core of E, spiral (S) galaxies form also their bulges at high redshift mainly by mergers. Mergers cannot play a significant role in the formation of disks since major mergers can destroy disks (Toomre & Toomre 1972; Hopkins et al. 2009), although recent simulations show cases where new disks soon regrow (Baugh et al. 1996; Steinmetz & Navarro 2002; Springel & Hernquist 2005; Athanassoula et al. 2016). Thin disks are thought to be formed from haloes with more quiescent merging history that accrete cool gas and gradually form stars with a radial distribution around the central bulge set by the angular momentum distribution of the halo (Neistein et al. 2006; Birnboim et al. 2007; Dutton et al. 2010). Both pictures suggest an inside-out view for the formation of a galaxy (Mo et al. 1998; Avila-Reese & Firmani 2000; Pilkington et al. 2012; Aumer & White 2013).

The overall process for the formation of galaxies is more complex, because the mass growth is not driven solely by gas supply. Other mechanisms like feedback from supernovae or Active Galactic Nucleus (AGN) are required to decouple the star formation from the gas accretion and to stop the growth of the galaxy (Croton et al. 2006; Dekel et al. 2009; Lilly et al. 2013). Furthermore, the morphological transformation following the formation of a spheroidal component can stabilize the gas disk against fragmentation and stop the growth of the galaxy (Martig et al. 2009; Genzel et al. 2014; González Delgado et al. 2015).

* http://califa.caha.es

In contrast, many spirals like the Milky Way (MW) do not harbor a classical bulge (Fisher & Drory 2010; Di Matteo et al. 2014), and instead they have a central thick disk (Haywood et al. 2013, 2015) that may have formed by clumpy instabilities in the star forming disk (Elmegreen et al. 2008). Some samples of galaxies at a redshift of ∼2 show clumpy star forming disks (Elmegreen et al. 2007; Genzel et al. 2008; Förster Schreiber et al. 2011; Wuyts et al. 2013), which suggest the formation of an early build up of pseudo-bulges by secular evolution. These results provide evidence for a modification of the inside-out formation scenario. In this line, van Dokkum et al. (2013) analyzed a sample of MW-like spirals at $z \sim 2.5$ and found that the mass growth took place in a fairly uniform radial way, since the size – stellar mass ($M_\star$) relation at $z \sim 2.5$ is similar to the relation at $z = 0$. Moreover, other mechanisms, such as stellar migration, bar-induced gas inflows, and angular momentum loss due to reorientation of the disk, can alter the inside-out view of the formation of a galaxy (Aumer et al. 2014).

Observational evidence in favor of the inside-out growth of star forming galaxies at high redshift already exists. For example, Nelson et al. (2016, 2012) have found that the Hα distribution of star forming galaxies at $z \sim 1$ is more extended than the stellar continuum, consistent with an inside-out assembly of the galactic disks. Other evidence comes from the radial mass structure of galaxies at $0.5 < z < 2.5$ that shows that the half mass radius (HMR) is on average 25% smaller than the half light radius (HLR). This result shows that galaxies are more compact in mass than in light, as a consequence of the inside-out mass growth of galaxies. The larger differences between the two radii occur in the most massive disk galaxies (Szomoru et al. 2010, 2012), in favor again of an inside-out formation scenario for disk galaxies.

In the local universe, further evidence of the inside-out formation scenario for spirals comes from the UV extended disks (Gil de Paz et al. 2005, 2007) detected by GALEX (Martin et al. 2005), and the radial distribution of the specific star formation rate (Muñoz-Mateos et al. 2007). However, recently it has been shown that spirals grow in size at a rate which is 0.35 times the rate at which they grow in mass (Pezzulli et al. 2015).

Theoretically, an inside-out formation process is expected for disks where they should increase in size while they grow in mass. Since the stars are distributed in a rotating disk and the specific angular momentum increases outwards, the inner parts should form earlier than the outer parts (Larson 1976; Brook et al. 2006, 2012; Pilkington et al. 2012).

This topic has achieved significant progress in the last years thanks to the ability of integral field spectroscopy (IFS) surveys (e.g., CALIFA, Sánchez et al. 2012a; MaNGA, Bundy et al. 2015) and the fossil record method (Tinsley 1968) to recover the information of the spatially resolved star formation history of nearby galaxies, and to derive the mass assembly history as a function of radial distance. CALIFA is well suited for these studies thanks to the large field of view and the spatial resolution of the instrument. The radial structure of the stellar ages and mass-growth curves can be obtained out to distances larger than 2 HLR and with a spatial sampling of ∼0.1−0.2 HLR. Moreover, the large sample of galaxies of the CALIFA survey that covers all Hubble types (Walcher et al. 2014), and galaxy stellar mass from 10^9 to $\sim 10^{12}$ $M_\odot$ (González Delgado et al. 2015) allow us to test the inside-out scenario for E, S0, and spirals from Sa to Sd, and low- to high-mass galaxies.

From the CALIFA survey, we have already obtained interesting results that favor the inside-out formation scenario. They are as follows: 1) from the mass assembly history of ∼100 galaxies (Pérez et al. 2013), we found that galaxies with $M_\star > 10^{10}$ $M_\odot$ grow inside-out, and the signal of downsizing is spatially preserved, with both inner and outer regions growing faster for massive galaxies. 2) From the ratio of the HMR to the HLR we found that these galaxies are more compact in mass than in light, supporting again the inside-out scenario (González Delgado et al. 2014b, 2015). 3) From the radial profiles of the stellar ages of ∼300 galaxies, we found negative age gradients for early- and late-type galaxies, confirming again the inside-out formation for E and spiral galaxies (González Delgado et al. 2015). This conclusion was also sustained by Sánchez-Blázquez et al. (2014) for a similar study based in a sub-sample of face-on disk CALIFA galaxies. 4) Using a completely different methodology, the study of the gas abundance gradients also suggests this inside-out scenario (Sánchez et al. 2012b, 2014; Sánchez-Menguiano et al. 2016; Marino et al. 2016).

Nonetheless, recent results from the MaNGA survey find more divergence in their conclusions: 1) from the mass assembly history, Ibarra-Medel et al. (2016) obtained that the innermost regions formed stars on average earlier than the outermost ones, supporting an inside-out formation scenario for ∼500 galaxies with $M_\star$ from $10^{9.3}$ to $10^{11.2}$ $M_\odot$. Their conclusion is independent of galaxy color, specific star formation rate (sSFR), and morphological type. 2) By using a similar set of data, Zheng et al. (2017) found slight negative age gradients, that point to an inside-out formation process for ∼1100 galaxies, half of which have Sersic index $n < 2.5$ (disk-like), and the other half of the sample have $n > 2.5$ (elliptical-like). 3) In contrast, for a similar set of data, but using different methods to retrieve the stellar population properties Goddard et al. (2017) found a positive age gradient for the early-type galaxies, suggesting an outside-in formation process for these galaxies. They both did full spectral fitting, but with different codes; Zheng et al. (2017) with STARLIGHT (Cid Fernandes et al. 2005), and Goddard et al. (2017) with FIREFLY (Wilkinson et al. 2015). They also use different stellar population models. Thus, their conclusions differ and seem to depend on the method of the analysis and the tracer (mass growth curve vs. age gradients) used to test the formation process.

In this paper, we analyze the complete set from the 3rd CALIFA data release (Sánchez et al. 2016), and test the results from three different tracers: 1) mass growth curves; 2) ratio of HMR to HLR; 3) age radial profiles (weighted in mass) of the stellar populations. This analysis will allow us to complement our previous results for a large sample of galaxies. Furthermore, in previous studies (Pérez et al. 2013; González Delgado et al. 2014b, 2015), we did not conclusively prove that galaxies with $M_\star < 10^{10}$ $M_\star$ form inside-out due to the poor statistics in this range of stellar mass. Now, the CALIFA extension sample will test the inside-out scenario for a large sample of galaxies, using a systematic analysis in the context of the three different diagnostic tracers mentioned above, as a function of Hubble type, stellar mass ($M_\star$), and stellar mass surface density ($\Sigma_\star$).

This paper is organized as follows. In Sect. 2, we describe the observations and data. In Sect. 3 we summarize the stellar population analysis, methodology, and sample distribution. Section 4 presents the two-dimensional (2D) radial stellar mass growth maps, the spatial averaged mass assembly and characteristic mass assembly epoch results. Section 5 discusses the ratio of half-mass to half-light radii as function of Hubble type, $M_\star$, and $\Sigma_\star$. Section 6 presents the mass-weighted age radial profiles. In Sect. 7 we discuss the global mass assembly time scales, their multivariate dependence and the mass-weighted age profiles both as a function of HLR and HMR. Finally, Sect. 8

summarizes the results of the paper and our main conclusions. Throughout we assume a flat ΛCDM cosmology with $\Omega_M = 0.3$, $\Omega_\Lambda = 0.7$, and $H_0 = 70$ km s^{-1} Mpc^{-1}.

2. Data and sample

2.1. Data

CALIFA (the Calar Alto Legacy Integral Field Area survey, Sánchez et al. 2012a) is an Integral Field Spectroscopy (IFS) survey designed to obtain spatially resolved spectra for 600 galaxies in the local Universe. Observations were carried out with the 3.5 m telescope at Calar Alto observatory with the Postdam Multi Aperture Spectrograph (PMAS, Roth et al. 2005) in the PPaK mode (Verheijen et al. 2004). PPak contains a bundle of 331 science fibers, each of 2.7″ in diameter, and a 71″ × 64″ field of view (FoV; Kelz et al. 2006). A three-pointing dithering is used for each object in order to reach a filling factor of 100% across the entire FoV. The observations were planed to observe each galaxy with two different overlapping setups. The low-resolution setup (V500; $R \sim 850$) covers from 3745 to 7500 Å with a spectral resolution of ∼6 Å FWHM, while the medium resolution setup (V1200; $R \sim 1650$) covers the blue part in the range 3400−4840 Å with spectral resolution of ∼2.3 Å FWHM. The spatial sampling of the datacubes is 1″/spaxel with an effective spatial resolution of ∼2.6″ FWHM.

2.2. Sample

The CALIFA mother sample was drawn from the SDSS DR7 (Abazajian et al. 2009) photometric galaxy catalog to obtain a representative and statistically significant sample of galaxies in the nominal redshift range $0.005 < z < 0.03$, fully described in Walcher et al. (2014).

We have used the full sample of the final CALIFA DR3 (Sánchez et al. 2016, hereafter DR3), with a total of 646 galaxies observed in the V500 grating. The DR3 release is the combination of two samples. The CALIFA Main Sample (MS) consists of galaxies belonging to the CALIFA mother sample, with a total of 542 in the V500 included in the DR3. The rest of the galaxies belong to the CALIFA Extension Sample, a set of galaxies observed within the CALIFA collaboration as part of different ancillary science projects (see DR3). They were reduced with the v2.2 CALIFA pipeline. The total number of datacubes in the V500 is 700, after adding all the galaxies from the ancillary science projects that have SDSS-DR7 images. We excluded type-1 Seyferts and galaxies that show merger or interaction features. This leaves a final sample of 661 galaxies.

DR3 galaxies were morphologically classified by five members of the collaboration through visual inspection of the SDSS *r*-band images, averaging the results as described in Walcher et al. (2014). We performed a similar classification procedure for the objects from the ancillary science projects.

As in previous works, we group the galaxies in seven morphology bins: E (120 galaxies), S0 (78, including S0 and S0a), Sa (94, including Sa and Sab), Sb (100), Sbc (93), Sc (110, including Sc and Scd), and Sd (66, including Sd, Sm, and Irr).

3. Stellar population analysis

3.1. Method of analysis

The stellar population properties are derived from the datacubes following the same methodology applied in previous works (Pérez et al. 2013; Cid Fernandes et al. 2013, 2014; González Delgado et al. 2014b,a, 2015, 2016). In short, the work-flow comprises three major steps. First, the preprocessing is done via QBICK, which includes spatial masking for foreground and background sources and masking of bad wavelength elements (large and small errors, bad pixels, ...). All spaxels within the isophote level where the average signal-to-noise ratio ≥3 (S/N) are spatially binned (if required) via Voronoi binning[1] (Cappellari & Copin 2003) so the final spectra achieve $S/N \gtrsim 20$. The coadded error spectra are corrected taking into account the correlation given by Sánchez et al. (2016)[2]. In the second step, the resulting spectra are fitted with STARLIGHT using the cluster at the Instituto de Astrofísica de Andalucía. Finally, the output is packed and processed using PyCASSO[3] (Cid Fernandes et al. 2013; de Amorim et al., in prep.).

The main difference with previous works is the updated base used in STARLIGHT to perform the full spectral fit. It consists of a combination of 254 SSP. For ages younger than 60 Myr we use the GRANADA models of González Delgado et al. (2005). For older ages, the SSPs are from Vazdekis et al. (2015) based on BaSTi isochrones. The *Z* range covers eight metallicities ($\log Z/Z_\odot = -2.28, -1.79, -1.26, -0.66, -0.35, -0.06, 0.25$ and $+0.40$). The age is sampled by 37 SSPs per metallicity covering from 1 Myr to 14 Gyr. The initial mass function (IMF) is Salpeter. Dust effects are modeled as a foreground screen with a Cardelli et al. (1989) reddening law with $R_V = 3.1$.

Table 1. Number of galaxies in each Hubble type and mass interval.

log M_* [$M_\odot$]	E	S0	Sa	Sb	Sbc	Sc	Sd	Total
8.4–9.9	12	1	1	6	4	44	42	110
9.9–10.4	5	6	7	11	21	40	20	110
10.4–10.8	12	11	16	22	29	18	3	111
10.8–11.1	14	24	17	27	23	4	1	110
11.1–11.3	21	22	31	20	14	2	0	110
11.3–12.0	56	15	21	14	2	2	0	110
Total	120	78	94	100	93	110	66	**661**

3.2. Stellar masses

The galaxy stellar masses ($M_\star$) used in this work are obtained by adding the masses of each individual spatial zone. This method takes into account variations in the stellar extinction and other stellar population properties, something that cannot be done with the integrated spectra. Masked areas due to foreground and background objects are filled in PYCASSO using the stellar mass surface density ($\Sigma_\star$) radial profile (see González Delgado et al. 2014b).

One of our chief aims is to derive the mass growth (MG) as a function of time and explore how these histories relate to other parameters, in particular Hubble type, stellar mass ($M_\star$), and stellar mass surface density ($\Sigma_\star$). Table 1 shows the distribution of galaxies by Hubble type and mass bins. The most populated Hubble type bins are E, Sb and Sc galaxies, while the Sd bin contains the fewest objects (66). We have computed the sextiles (6-quantiles) of the stellar mass range of the whole sample

[1] Measured in a 90 Å window centered at 5635 Å rest-frame.
[2] See Appendix of García-Benito et al. (2015) for a description of the procedure.
[3] The Python CALIFA STARLIGHT Synthesis Organizer.

in order to divide the sample into six bins (of stellar mass), each with almost the same number of objects.

The upper panel of Fig. 1 shows the distribution of $M_\star$ as a function of Hubble type. As seen from the median value of each bin (inner dot in the boxplot inside the violin plots), mass correlates with Hubble type. Early-type galaxies (E, S0, and Sa) on average have $M_\star \geq 10^{11}$ $M_\odot$ while latter spirals like Sd have $M_\star \leq 10^{9.6}$ $M_\odot$. However, the distribution of some Hubble types shows a significant coverage in mass. Ellipticals (E), although concentrated in the high-mass end as seen from the shape of the violin plot, have a small tail all the way down to 10^9 $M_\star$. This is the result of an ancillary project which was looking to populate this Hubble type and mass regime. To a lesser extent, late spirals (Sc, Sd) also show a broader distribution than other types as seen from their slightly larger interquartile ranges. These late spirals, 54% of them coming from ancillary projects (59 out of 110), populate the low-mass end below the completeness limit of the CALIFA survey[4] ($9.9 \leq \log M_\star\ (M_\odot) \leq 11.7$).

3.3. Stellar mass surface density

The total stellar mass is an important parameter in star formation and chemical enrichment in spheroids. However, it is in disks where stellar mass surface density comes into play, as seen by the local relations between $\Sigma_\star$ and mean metallicities (González Delgado et al. 2014a) and between $\Sigma_\star$ and stellar ages (González Delgado et al. 2014b).

In a previous work using 107 galaxies from the CALIFA survey, González Delgado et al. (2014b) showed that several galaxy-averaged properties, in particular $\Sigma_\star$, correlate nicely with the mean value over a ring at 1 ± 0.1 HLR from the nucleus. We have estimated the galaxy-averaged $\Sigma_\star^{\rm galaxy}$ in the same way, dividing the total mass (summing the total area of each spaxel, A_{xy}) by the total area of these spaxels:

$$\Sigma_\star^{\rm galaxy} = \frac{\Sigma_{xy} M_{xy}}{\Sigma_{xy} A_{xy}}. \quad (1)$$

Figure 2 shows this relation for 661 galaxies. The local value at 1 HLR follows nicely the one-to-one line except for the upper end of $\Sigma_\star^{\rm galaxy}$, where $\Sigma_\star^{\rm galaxy}$ is on-average lower than $\Sigma_\star^{\rm HLR}$ and it correlates better at 1.1−1.2 HLR.

From now on, we will use the local value of $\Sigma_\star$ at 1 HLR ($\Sigma_\star \equiv \Sigma_\star{}^{1\ \rm HLR}$). In the same way as with the total stellar mass $M_\star$, we have computed the sextiles of $\Sigma_\star$ in order to divide the sample into six equally populated bins, as shown in Table 2.

The middle panel of Fig. 1 shows the distribution of $M_\star$ as a function of our $\Sigma_\star$ bins. For the two highest $\Sigma_\star$ bins (2.8 to 3.7 $M_\odot$ pc^{-2}), the median stellar mass is nearly the same, indicative of fairly compact mass distribution, with their interquartile range between $10^{10.8}$ $M_\odot$ and $10^{11.3}$ $M_\odot$. The rest of the $\Sigma_\star$ bins show a more spread distribution in mass, with a correlation for their median values between $M_\odot$ and $\Sigma_\star$, that mimics that of the total mass and Hubble type distribution (upper panel, Fig. 1).

The distribution of $\Sigma_\star$ as a function of Hubble type is shown in the bottom panel of Fig. 1. At first sight it resembles that of $M_\star$. Despite ellipticals spanning over a large $\Sigma_\star$ range, most of them peak close to the high end ~2.8 $M_\odot$ pc^{-2}. However, a clear difference with the mass distribution is the turning point in the correlation for S0 galaxies. These galaxies peak at a higher $\Sigma_\star$ value close to 3 $M_\odot$ pc^{-2}, while for the mass, we have seen

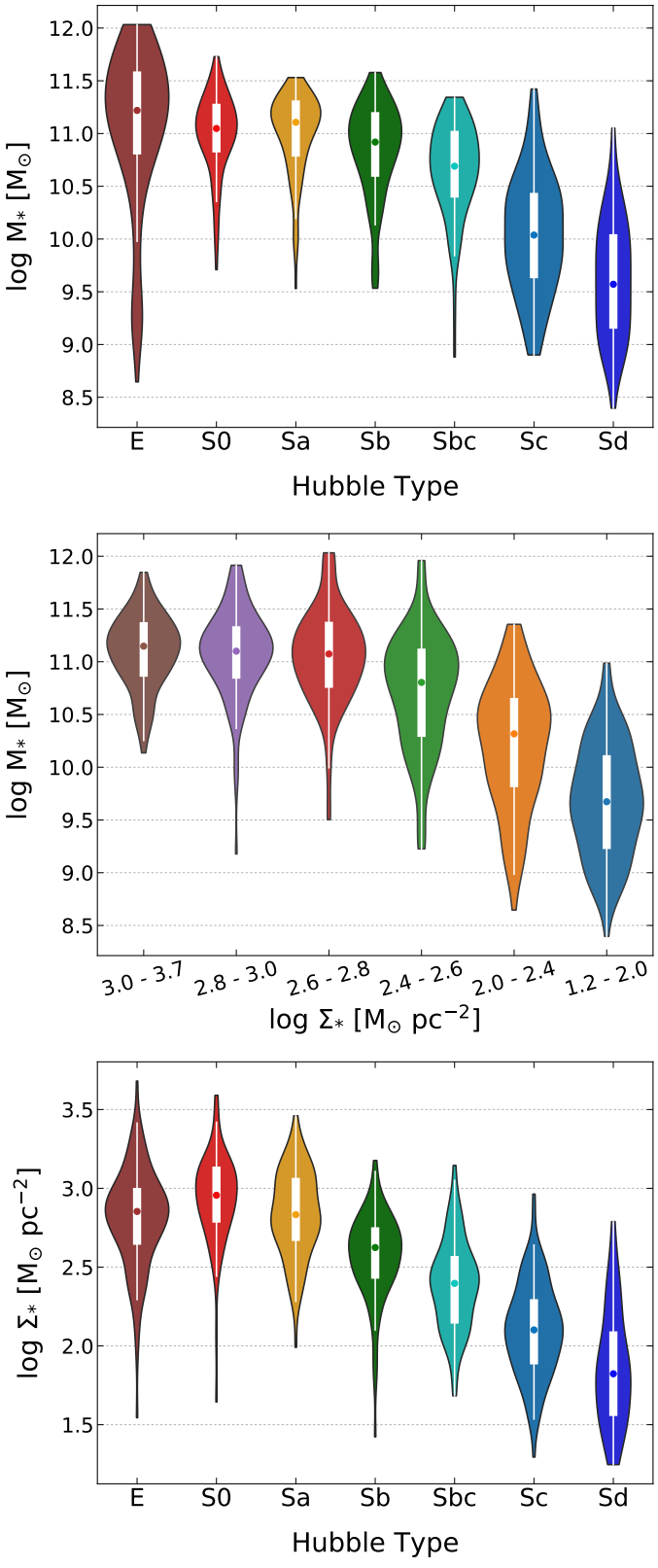

Fig. 1. Violin plots of the stellar masses for each Hubble type (*upper panel*), stellar masses for each stellar mass surface density bin (*middle panel*), and stellar mass surface density for each Hubble type (*bottom panel*). Its corresponding box plot showing the interquartile range is plotted inside each violin plot. The inner dot in the box plot represents the median of the distribution. The values of the stellar mass surface density were obtained at 1 HLR (see Sect. 3.3). The width of the "violins" are scaled by the number of observations in each bin.

[4] The limits of the mother sample provided by Walcher et al. (2014) are scaled to Salpeter IMF.

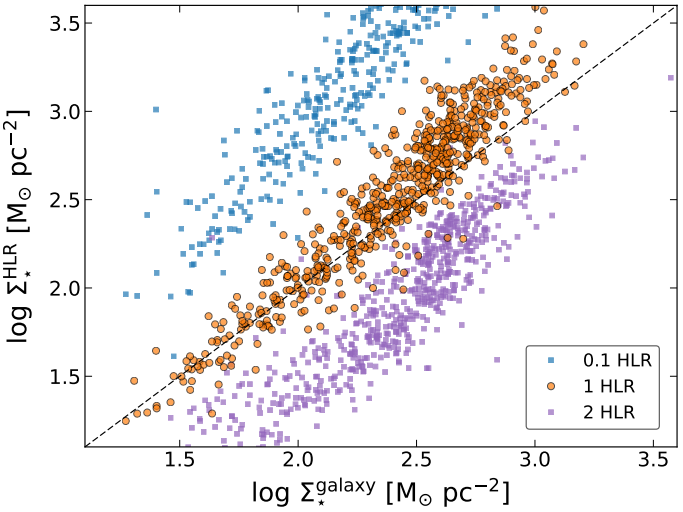

Fig. 2. Relation between log $\Sigma_\star^{\rm galaxy}$ and the stellar mass surface density mean value over a ring of 0.1 HLR width at 0.1 HLR, 1 HLR, and 2 HLR from the nucleus. The dashed black line shows the one-to-one relation.

Table 2. Number of galaxies in each total mass and stellar mass surface density interval.

log M_* [$M_\odot$]	log $\Sigma_\star$[$M_\odot$ pc^{-2}]						Total
	1.2	2.0	2.4	2.6	2.8	3.0	
	2.0	2.4	2.6	2.8	3.0	3.7	
8.4–9.9	69	31	6	2	2	0	110
9.9–10.4	36	35	25	4	4	6	110
10.4–10.8	3	29	24	24	15	16	111
10.8–11.1	2	8	26	24	25	25	110
11.1–11.3	0	6	16	26	33	29	110
11.3–12.0	0	2	13	30	31	34	110
Total	110	110	111	110	110	110	**661**

that Sa galaxies are the ones that, on average, have slightly larger values. The remaining spirals follow a similar rank relation to that of the mass (left panel).

4. Spatially resolved mass-growth histories

4.1. Radial stellar mass-growth 2D maps

Following the space × time diagrams ($R \times t$) introduced by Cid Fernandes et al. (2013; see their Fig. 12), we apply the same representation scheme to the mass growth of galaxies. These diagrams show in the x-axis the lookback time, while the y-axis is the radial distance, compressing the xy information into R, producing radially averaged maps of the desired quantity.

Figure 3 shows the $R \times t$ maps of the mass assembly, a means to represent the mass growth history of galaxies in 2D. STARLIGHT provides a wealth of information for each single spectrum, in particular the mass in stars for each mass fraction vector m_{xytZ}, derived by STARLIGHT from the population vector taking into account the stellar extinction and M/L spatial variation. This vector is collapsed in the metallicity (Z) axis, and then the cumulative mass function along the time axis is computed for each spatial location. The cumulative function for a given spaxel is calculated by adding all mass formed up to a given lookback time and dividing by the final stellar mass. In order to stack any given property, galaxy by galaxy, we express the distance in a common metric such as the HLR, the semi-major axis length of the elliptical aperture which contains half of the total light of the galaxy at the rest-frame wavelength 5635 Å. Radial apertures of 0.1 HLR in width were used to extract the radial profiles.

The averaged mass growth 2D maps of 661 galaxies in 6 $M_\star$ bins and 6 $\Sigma_\star$ bins is shown in Fig. 3. The maps contain also the relative stellar mass growth curve of three spatial regions: inner 0.5 HLR (solid line), 1.5 ≤ HLR ≤ 2 (dashed line), and total (dash-dotted line). The mass growth curve for every component and galaxy is computed by averaging the spatial locations within the required distance and then the individual value is stacked for all galaxies. The standard error of the mean is estimated at every radial distance and for each spatial region. We show only averaged quantities with a minimum number of seven galaxies per bin (∼1% of the total sample). Both the 2D maps and spatial component curves show clearly the inside-out assembly of the stellar mass, which is preserved at any $M_\star$ and $\Sigma_\star$ bin and time, even for the low-mass end. The assembly of the mass in the outskirts of the galaxies is more extended in time than the inner 0.5 HLR. The averaged growth curve for the whole galaxy always keeps in an intermediate loci between inner and outer regions.

4.2. Spatial averaged mass assembly

We can collapse the results of Fig. 3 in both axes and stack also by Hubble type in order to assess the global shape of the mass assembly curves. Figure 4 shows the averaged results for three different spatial regions (≤0.5 HLR, 0.5 ≤ HLR ≤ 1, 1.5 ≤ HLR ≤ 2) and for the whole galaxy. We can see at work a stellar-mass ranking (upper panel) in the global curve, that is, archaeological downsizing[5], indicating that stars in more massive galaxies formed at an earlier epoch and in a shorter time span, confirming our previous result from the analysis of a sample of 105 galaxies (Pérez et al. 2013). The downsizing effect is also spatially preserved for different regions. The growth curve from the low to medium mass regime are well segregated, while the curves for the bins up to the higher-mass end display tighter ranking. It is worth noting that the first two bins cover two order of magnitudes in mass ($10^{8.4}$ to $10^{10.4}$ $M_\odot$) while the four upper mass bins cover a smaller range from ($10^{10.4}$ to $10^{12.0}$ $M_\odot$). By construction all bins contain the same number of galaxies.

The anti-correlation between the stellar mass surface density of galaxies and the formation epoch of the stars is preserved. Again, the first two lower bins span for over two orders of magnitude in $\Sigma_\star$ ($10^{1.2}$ and $10^{2.4}$), while the rest are concentrated between $10^{2.4}$ and $10^{3.7}$ $M_\odot$ pc^{-2} displaying a tighter ranking of the mass growth curves.

The cumulative mass fraction plots show that both $M_\star$ and $\Sigma_\star$ are fundamental parameters segregating the mass assembly curves. However, this is not the case for all morphological types, where the downsizing does not hold for early types (E and S0) at all epochs, albeit the ranking holds for the remaining Hubble types. On the one hand, we have seen that ellipticals span a significantly large mass range (upper panel, Fig. 1) and the median mass of Sa galaxies is slightly larger than S0 galaxies. On the other hand, S0 galaxies have, on average, largest stellar mass surface density values (bottom panel, Fig. 1) and also show a fairly broad $\Sigma_\star$ range. The combination of these factors seems to be reason for the break of the "top-down" mass assembly behavior for E and S0 galaxies.

[5] See Fontanot et al. (2009) for a summary of different types of downsizing.

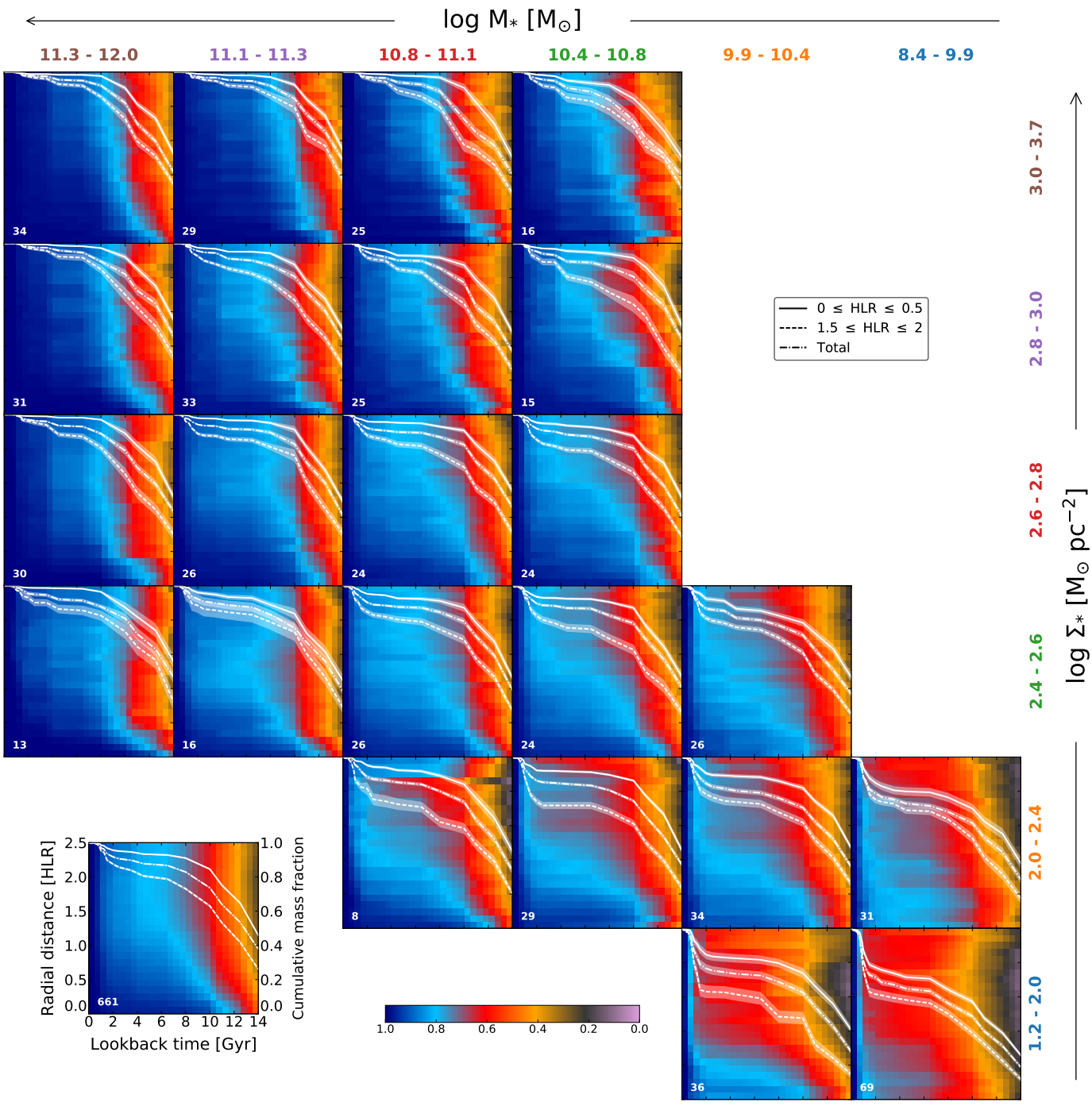

Fig. 3. Radial stellar mass growth maps up to 2.5 HLR stacked by stellar mass and stellar mass surface density. Each radial bin is normalized to its final $M_\star$. Lines overplotted on the 2D maps represent the relative stellar mass growth of three main spatial regions (white): inner 0.5 HLR (solid line), 1.5 ≤ HLR ≤ 2 (dashed line), and total (dash-dotted line). The (white) shaded areas represent the standard deviation of the mean. The lower left number in each map indicates the number of galaxies stacked for that particular bin. The *lower-left inset box* shows the results for all 661 galaxies. Mass and stellar mass surface density bins grow *from right to left and bottom to top*, respectively.

4.3. Characteristic mass assembly epoch

For all stellar mass and stellar mass surface density bins, the average 2D maps show a clear inside-out mass growth. To better quantify the rate at which the galaxies have grown their mass, we compute the epoch where 80% of the total assembled mass (t_{80}) for each spatial region was built. We choose two distinct regions: ≤0.5 HLR representative of the inner part and 1.5 ≤ HLR ≤ 2 for the outer component. Figure 5 displays the distribution of stellar mass assembly ages in bins of $M_\star$ and $\Sigma_\star$. We have not stacked the individual values in each bin, to better visualize the differences and scatter of the samples by means of box plots. The interquartile range shows a clear difference: outer regions achieve their 80% stage at a more recent epoch that inner regions. In most cases, the interquartile ranges are well separated for both regions, an indication of two different assembly ages. Also, the assembly epoch for the outer regions presents more scatter in the intermediate $M_\star$ and $\Sigma_\star$ bins.

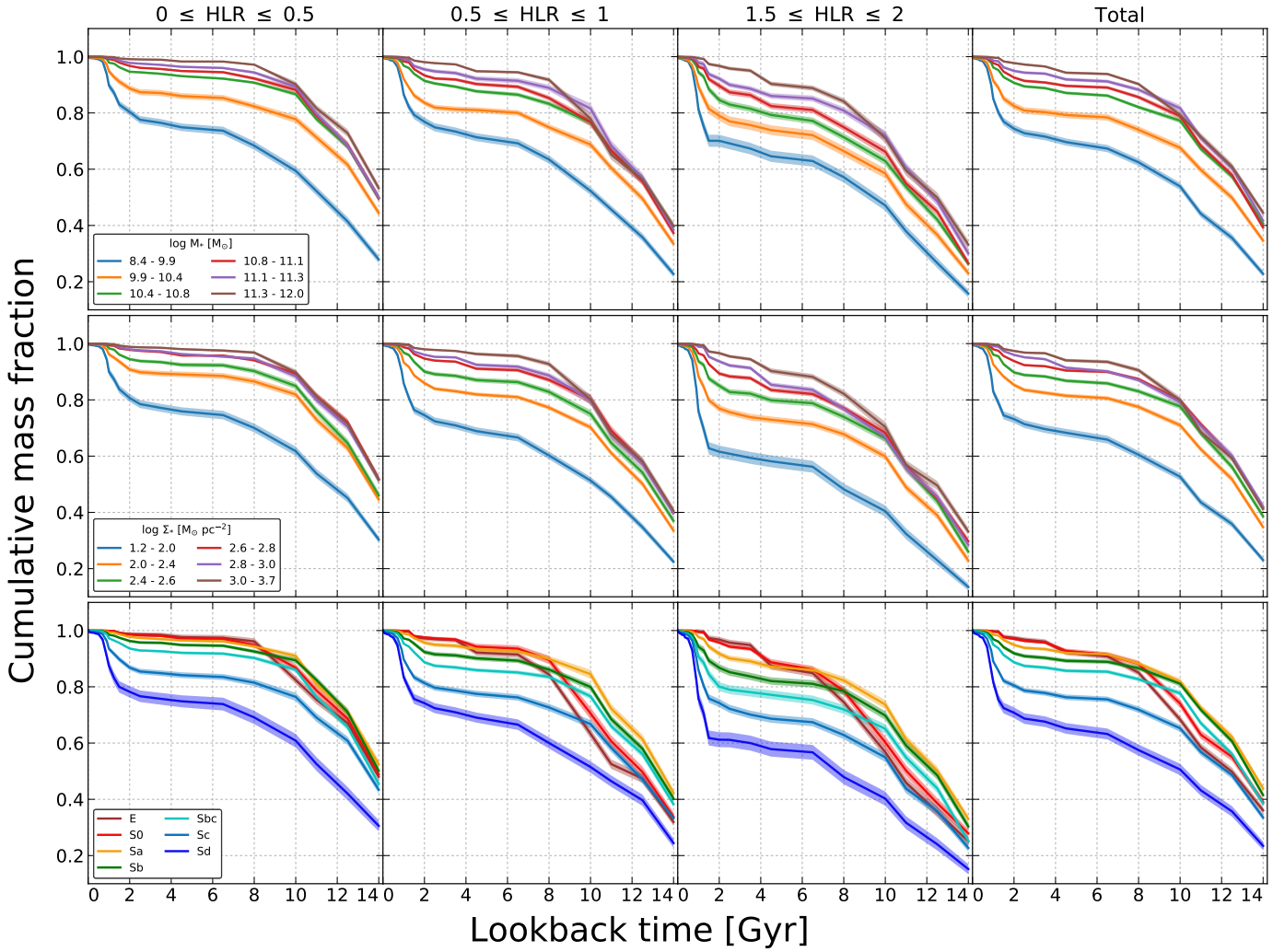

Fig. 4. Relative stellar mass growth of three spatial regions (≤0.5 HLR, 0.5 ≤ HLR ≤ 1, 1.5 ≤ HLR ≤ 2) and total, binned by stellar mass (*upper panel*), stellar mass surface density (*middle panel*) and Hubble type (*lower panel*).

The median values (gray line inside the boxplots) for the ages of the inner region populations are systematically older than the outer ones; a signal that the "downsizing" effect is spatially preserved. The largest difference for the median values of t_{80} between inner and outer regions is found for bin (10.4−10.8, 2.0−2.4) [log $M_\star$, log $\Sigma_\star$], where the inner region formed 80% of its mass 9.2 Gyr before the outer region, followed by and (10.8−11.1, 2.0−2.4) [log $M_\star$, log $\Sigma_\star$] (8.6 Gyr) and (9.9−10.4, 2.0−2.4) [log $M_\star$, log $\Sigma_\star$] (8.6 Gyr). It is worth noting all three cases belong to the same (2.0–2.4) [log $\Sigma_\star$] bin. As for the smaller differences between inner and out regions, these are found in bins (8.4−9.9, 1.2−2.0) [log $M_\star$, log $\Sigma_\star$] (0.5 Gyr) and (8.4−9.9, 2.0−2.4) [log $M_\star$, log $\Sigma_\star$] (1.7 Gyr), at the lowest $M_\star$ and $\Sigma_\star$ ranges.

For a quantitative proof of the inside-out mass growth mechanism, we conducted statistical tests for comparing these two populations medians. The Paired t-Test is valid when the number of pairs is >30, or when the *differences* of the pairs follow a normal distribution (for number of pairs <30), and it does not assume that the groups are homoscedastic. In case these assumptions are not met, a non-parametric paired difference test can be used, like the Wilcoxon signed-rank test. We have conducted both tests for all samples in Fig. 5 and both conclude that the paired population means are not equal, and therefore, the assembly ages for the inner regions are larger than the outer regions for *all* $M_\star$ and $\Sigma_\star$ bins.

As we did for the mass assembly curves, we can collapse Fig. 5 in both axes. Figure 6 shows the results comparing the characteristic mass assembly at t_{80} collapsing by $M_\star$, $\Sigma_\star$ and Hubble type for the (≤0.5 HLR) and outer (1.5 ≤ HLR ≤ 2) regions. Each bin now includes all 661 galaxies. Again, the median values of the outer regions is always below that of the inner region, for every $M_\star$, $\Sigma_\star$, and Hubble type bin, as is also the case for most of the interquartile range; an indication that, on average, the inner parts form earlier than the outer parts of the galaxy. The spread in the values of t_{80}, judged from the interquartile range in the box plots, is, in general, larger in the outer regions. This is also particularly evident from the relative wider interquartile range for the (9.9–10.4) [log $M_\star$] bin and (2.0–2.4) [log $\Sigma_\star$] and (1.2–2.0) [log $\Sigma_\star$] bins of the inner regions (left panel).

The median t_{80} epoch for the inner regions is very similar for the four higher-mass bins (left panel, 10.4 to 12.0 log $M_\star$), with values of 11.2 Gyr for the higher-mass bin and ∼10.7 Gyr for the other three. A similar behavior is displayed in the $\Sigma_\star$ bins (middle panel). The outer region, both for $M_\star$ and $\Sigma_\star$, shows a more pronounced top-down sequence. As for the Hubble type (right

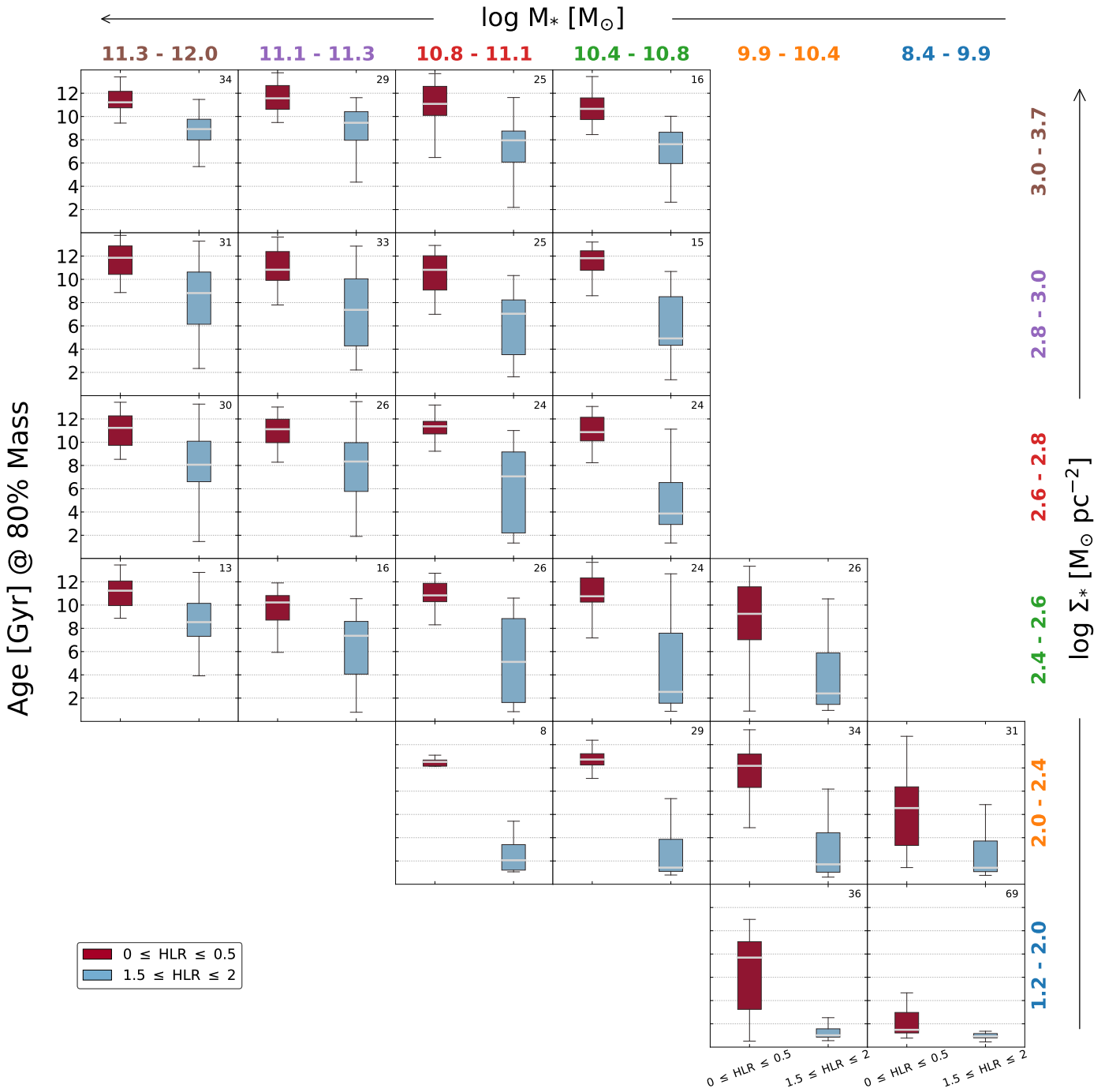

Fig. 5. Box plot diagram of the age (in Gyr) at which the inner (≤0.5 HLR) and outer (1.5 ≤ HLR ≤ 2) spatial regions grow to 80% of their final stellar mass stacked by stellar mass and stellar mass surface density. The gray horizontal line in each box plot shows the median of the distribution. The upper right number in each panel indicates the number of galaxies stacked for that particular bin.

panel), the ranking for the median values is not preserved either by the inner or outer regions. This trend is understandable in the light of Fig. 1, where we see a similar pattern in the $\Sigma_\star$ distribution as a function of Hubble type.

5. Half-mass versus half-light radius

So far we have used a galaxy metric based on their light, the HLR. However, stellar mass is a key parameter in describing the mass assembly, and therefore the HMR seems a more suitable physical metric for galaxy evolution. The relation between these two metrics depends on the variations of the SFH and/or extinction, which produce a spatially dependent M/L ratio.

Thanks to our spatially resolved SFH, we can obtain the relation between HLR and HMR. We estimate the latter using the 2D distribution of $\Sigma_\star$, defined as the semi-major axis length of the elliptical aperture which contains half of the total mass of the galaxy. Figure 7 shows their relation as a function of $M_\star$, $\Sigma_\star$, and Hubble type. The median half-mass size is always smaller than half-light radii for all three parameters. The lowest ratio is found in three of the most massive bins (10.4 to 11.1 log $M_\star$), where galaxies are 25% smaller in mass than in light, very similar to

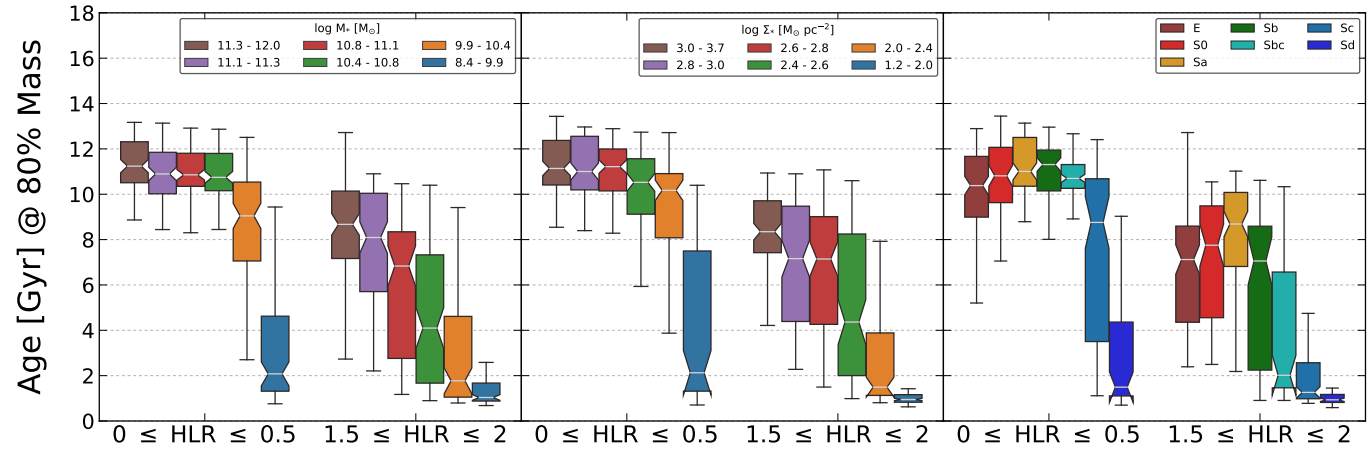

Fig. 6. Same as Fig. 5 but binning only in one property: stellar mass (*left*), stellar mass surface density (*center*), and Hubble type (*right*).

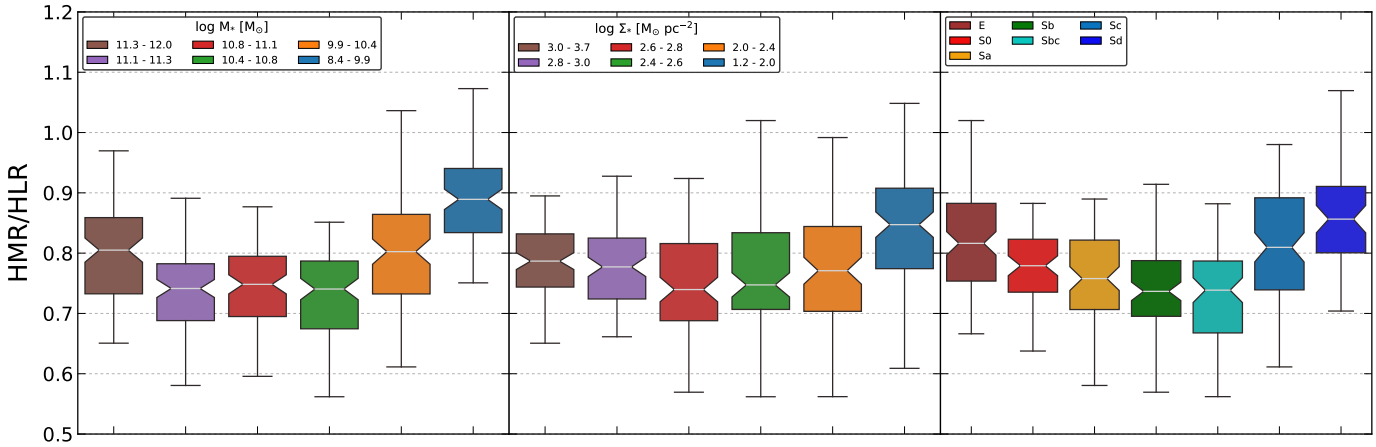

Fig. 7. Box plot diagram of the ratio between the half-mass and the half-light radius binned by Hubble type (*left*), stellar mass (*center*), and stellar mass surface density (*right*). The gray horizontal line in each notched box plot shows the median of the distribution.

the value found by Szomoru et al. (2013) for galaxies at $0.5 < z < 2.5$ with $>10^{10.7}$ $M_\odot$. Low-mass galaxies (8.4–9.9) [log $M_\star$] show the largest ratio with HMR/HLR ~ 0.89. The trend is also followed by $\Sigma_\star$, although the relation is less pronounced. As for the Hubble type, Sb and Sbc galaxies present the lowest HMR/HLR ratio (0.74), in accordance with our previous results (González Delgado et al. 2015).

The HLR was estimated in the observed light profiles. In previous works, we have presented detailed analysis of the several stellar profiles of several stellar properties, including the extinction (see González Delgado et al. 2015). Thanks to the 2D extinction maps we can explore whether dust correction could flatten the HMR/HLR. We corrected the light profiles using the extinction maps and estimated the HLR^{DeRed}. Extinction has a mild effect on the flattening of the HMR/HLR^{DeRed}. For the low-mass galaxies bin, the ratio flattens by 1%, while for the range (9.9–11.3) [log $M_\star$] the increase in the ratio is between 5% and 7%, being close to 3% for the most massive galaxies.

6. Mass-weighted age profiles

Following our previous definitions (Cid Fernandes et al. 2013), the mass-weighted mean log stellar age is defined as

$$\langle \log \text{ age} \rangle_M = \sum_{t,Z} m_{tZ} \times \log\, t, \qquad (2)$$

where m_{tZ} is the fraction of mass attributed to the base element with age t and metallicity Z.

In González Delgado et al. (2014b) we analyzed the radial profiles of the luminosity-weighted log stellar age $\langle \log \text{ age} \rangle_L$ as a function of mass and Hubble type and $\langle \log \text{ age} \rangle_M$ as a function of Hubble type for 300 galaxies. Figure 8 goes a step further and explores the $\langle \log \text{ age} \rangle_M$ radial profiles *both* as a function of $M_\star$ and $\Sigma_\star$for 661 galaxies. Because of the weight of old populations, $\langle \log \text{ age} \rangle_M$ spans a smaller dynamical range than light-weighted age. However, $\langle \log \text{ age} \rangle_M$ and its gradient is less affected by young populations whose contribution is negligible to the mass growth. Negative gradients are detected in all galaxies. The radial profiles of $\langle \log \text{ age} \rangle_M$ decrease outward for all bins, which are more pronounced for low-$M_\star$ and low-$\Sigma_\star$ galaxies, a clear effect of the inside-out growth of galaxies. The stellar mass surface density seems to play a role between galaxies of the same $M_\star$, with a general downsizing pattern particularly notable for low $M_\star$. Most of the stellar mass in the center was formed more than 10 Gyr ago, except for the lowest-$M_\star$ and -$\Sigma_\star$ bins. There is a general change in the trend around the spatial region 1–1.5 HLR, where the profile starts to flatten, although in a less noticeable manner for low-mass galaxies. The (10.8−11.1, 2.4−2.6) [log $M_\star$, log $\Sigma_\star$] bin has a $\langle \log \text{ age} \rangle_M$ radial profile representative of the whole sample, very close in shape and value to the global one.

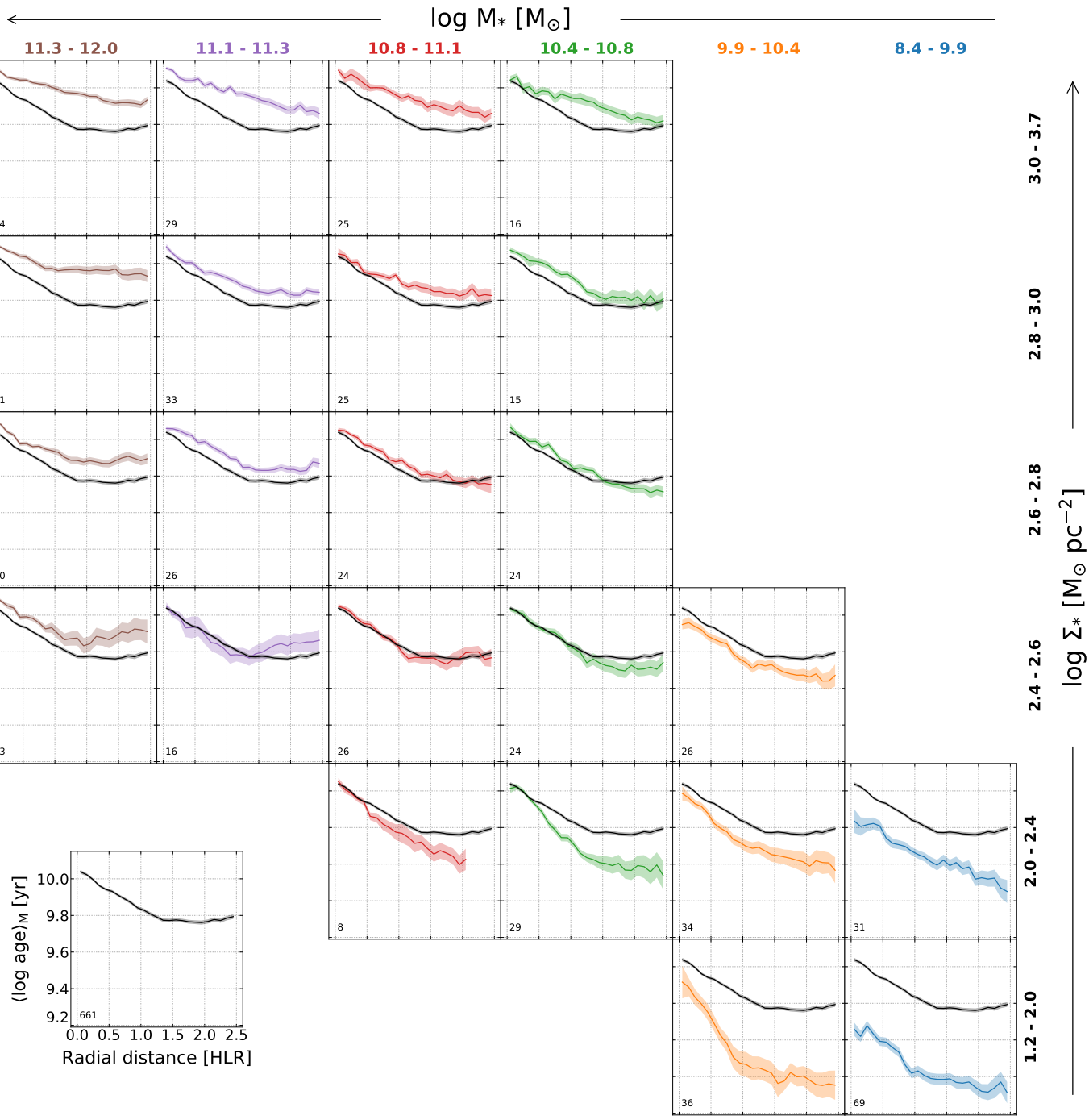

Fig. 8. Radial profiles (in units of HLR) of the mass-weighted age stacked by stellar mass and stellar mass surface density. The gray line shows the median profile obtained with the 661 galaxies. This profile is also shown in the lower-left inset box. The number of galaxies in each bin is indicated in the lower-left side of each panel.

7. Discussion

7.1. Global mass assembly time scales

The global mass assembly for the whole galaxy for different epochs is plotted in Fig. 9. The top-down trend is nicely followed by all mass bins (left panel) at all characteristic epochs, except for t_{80}, where the median of the second highest mass bin is slightly larger than the most massive bin. The downsizing effect for t_{90} is the more pronounced among these four epochs, albeit with an interquartile range that is larger for the intermediate mass bins. The global mass assembly for the stellar mass surface density (central panel) has a similar time scale for the highest bins, and the difference between bins increases also for t_{90}, where there is a clear top-down trend for the median values. The Hubble type follows a similar pattern to the spatially resolved case (Fig. 6), where the highest value is obtained by Sa galaxies.

So far we have considered the time scales at which the galaxy or a component of the galaxies attains a percentage of their mass. Another way of looking at the mass assembly is by slicing at a particular time and comparing the fractions of masses formed by that epoch. This is presented in Fig. 10 for $z = 1$ (~7.7 Gyr).

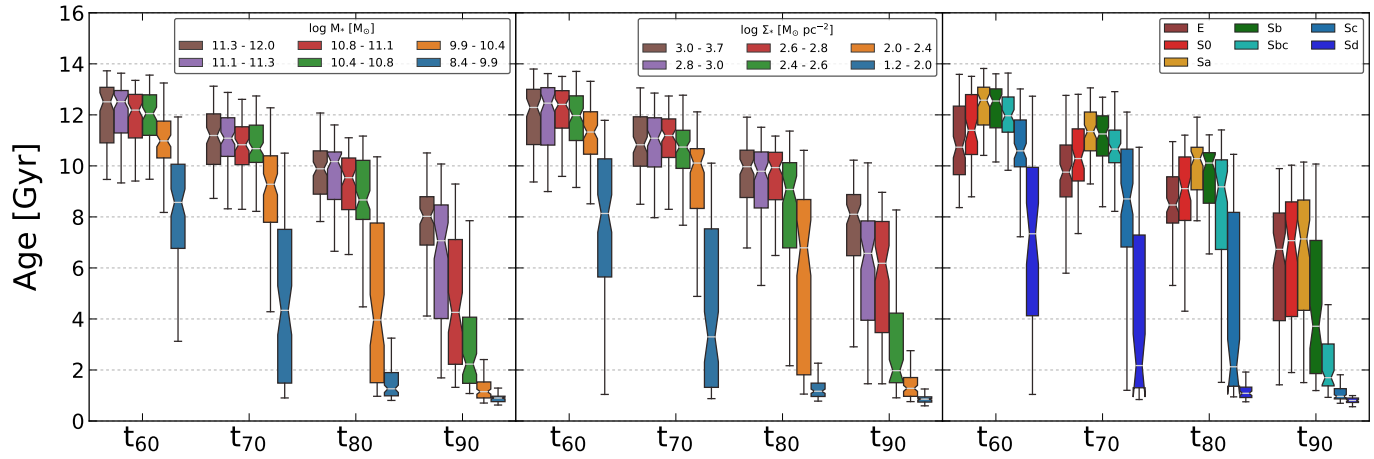

Fig. 9. Box plot diagram binning by stellar mass (*left*), stellar mass surface density (*center*), and Hubble type (*right*) of the age (in Gyr) at which the galaxies grow to 60%, 70%, 80%, and 90% of their final total stellar mass. The gray horizontal line in each notched box plot shows the median of the distribution.

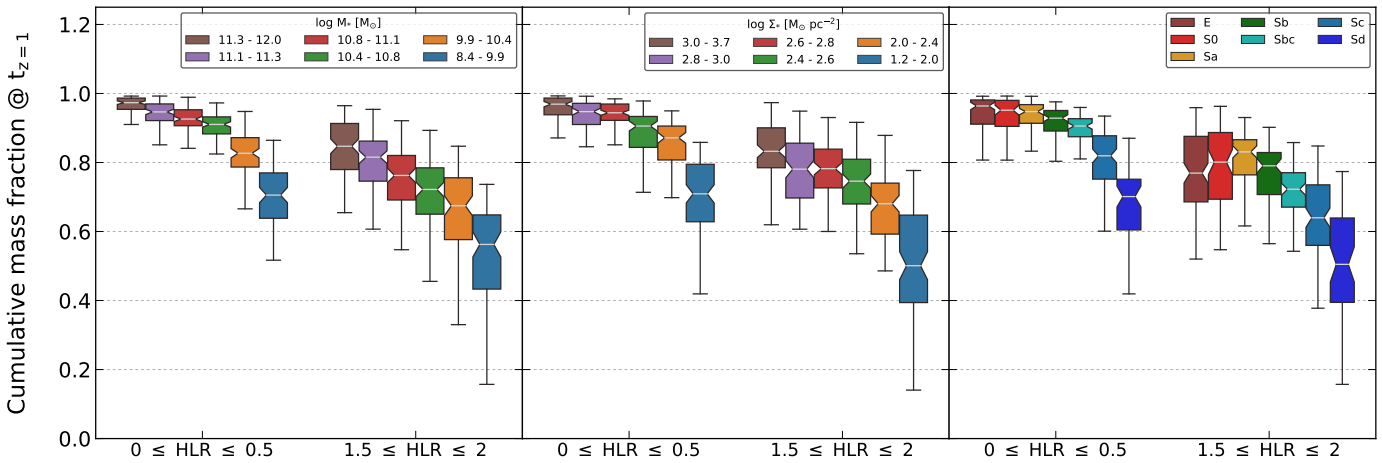

Fig. 10. Box plot diagram of the relative stellar mass growth for the inner (≤0.5 HLR) and outer (1.5 ≤ HLR ≤ 2) regions at $z = 1$ (~7.7 Gyr). The gray horizontal line in each notched box plot shows the median of the distribution.

Both the mass fraction of the inner (≤0.5 HLR) and outer regions (1.5 ≤ HLR ≤ 2) is shown for comparison. The spatially resolved downsizing pattern for the inner and outer regions is preserved both for $M_\star$ and $\Sigma_\star$. On average, the inner regions of the most massive galaxies ((11.3–12.0) [log $M_\star$]) have already attained almost all their mass at $z = 1$ (~97%), while the inner regions of low-mass galaxies ((8.4–9.9) [log $M_\star$]) are still at ~70% of their final mass. The outer regions follow a similar trend, although as noted previously, with slightly larger scatter, increasing towards low-mass galaxies. As seen in Sect. 7.2, the assembly rates of this mass regime seem to be strongly dependent on other parameters such as the Hubble type, leading to a higher scatter. The outer region of massive galaxies is at ~85% of its final mass at $z = 1$, while for low-mass galaxies this is ~56%. The stellar mass surface density mimics the spatially resolved downsizing pattern seen for the mass and their average cumulative fraction values. The situation changes for the Hubble type. The top-down pattern is followed for the inner regions from E to Sd galaxies, but this trend is broken for the outer parts, where again the peak is found for the Sa bin. This can be understood in light of the SFH of E and S0 galaxies. In González Delgado et al. (2017) we have found these galaxies to have an important active epoch of mass assembly at $z \sim 1$ in their outer parts (1–1.5 HLR).

7.2. Multivariate mass assembly

We have reported that the global and spatially resolved mass assembly of galaxies have a distinct behavior as functions of total stellar mass, stellar mass surface density and Hubble type. However within a bin of a particular parameter, galaxies can have different properties, and there might be secondary dependencies on one (or more) of these properties. In fact in González Delgado et al. (2015) we showed that radial variations in averaged light-weighted ages are modulated primarily by galaxy morphology, and only secondarily by the galaxy mass. We have seen at work in Figs. 3, 5, and 8 a segregation in both stellar mass and stellar mass surface density. Here we want to assess whether or not there is any dependence on some of the reported parameters.

In the left panel of Fig. 11, we present the distribution of the global t_{80} both as a function of stellar mass and stellar mass surface density bins. The number of galaxies in each bin is the same as in Table 2 and Figs. 3, 5, and 8. For galaxies in the first two lowest-mass bins (log $M_\star$ from 8.4 to 10.4), stellar mass surface density clearly segregates galaxies by formation epoch t_{80}, especially for the lowest stellar mass surface density bin (1.2–2.0) [log $\Sigma_\star$]. For intermediate-mass bins (log $M_\star$ 10.4 to 11.1),

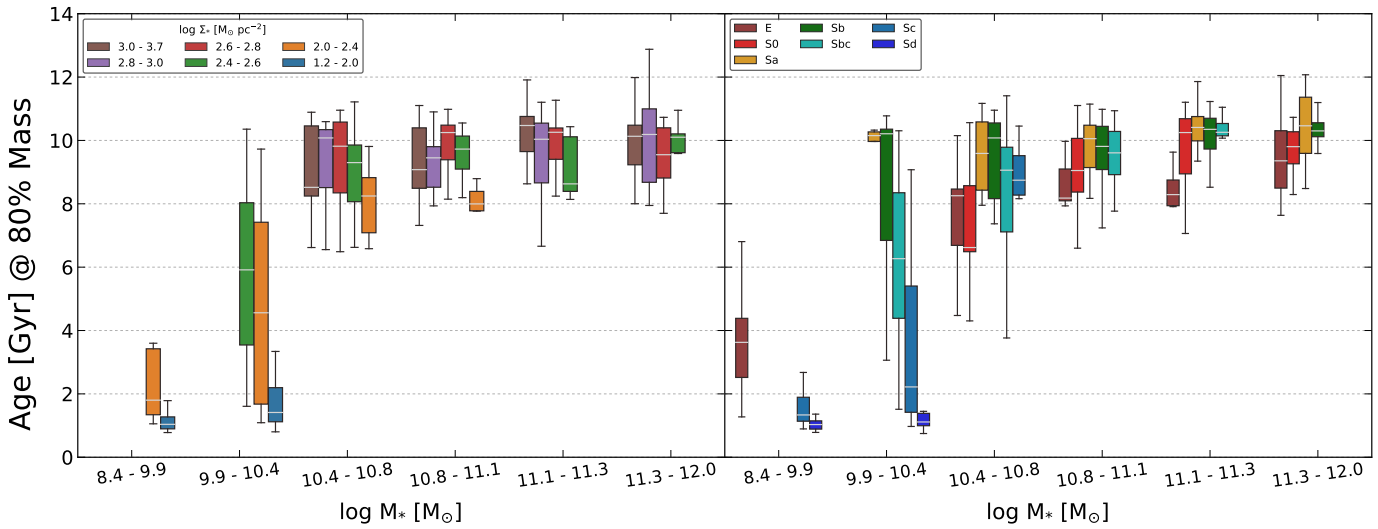

Fig. 11. *Left panel*: box plot diagram of the age (Gyr) at which the galaxies grow to 80% of their final stellar mass segregated by stellar mass surface density bins. *Right panel*: box plot diagram of the age (Gyr) at which the galaxies grow to 80% of their final stellar mass segregated by Hubble-type bins. The gray horizontal line in each box plot shows the median of the distribution.

stellar mass surface density seems to play a role for the lowest-$\Sigma_\star$ bin available in that stellar mass range ((2.0–2.4) [log $\Sigma_\star$]), but higher stellar mass surface density values appear to be insensitive in this regime and in the highest stellar mass bins.

The right panel of Fig. 11 displays the distribution of the global t_{80} both as a function of mass and Hubble type. As in previous figures, we show only bins with a minimum number of seven galaxies (see Table 1). For galaxies in the first two lowest-mass bins (log $M_\star$ from 8.4 to 10.4), Hubble type clearly segregates by formation epoch t_{80}. The scatter of (9.9–10.4) [log $M_\star$] seen in the left panel of Fig. 11 seems here to be related to the time scales of different morphological types in this mass range. For intermediate- and high-mass bins, there seems to be a slight dependence for early types (E and S0), whereas later types reach a "plateau" within each mass bin.

From this latter plot it is evident that low-mass galaxies and the low end of intermediate-mass galaxies (log $M_\star$ from 8.4 to 10.4) show a clear diversity in their assembly times, diversity that correlates with stellar mass surface density and strongly with Hubble type. These properties still have some effect on their time scales for higher-mass ranges, but the differences are milder. Using 105 CALIFA galaxies, Pérez et al. (2013) suggested an outside-in assembly formation for lower-mass galaxies. As we have seen, the assembly epoch is very diverse for low-mass galaxies, and thus their low statistics in this mass regime could have biased this result. Ibarra-Medel et al. (2016) also found a significant diversity on the assembly epochs for low-mass galaxies, although they only made a distinction between early- and late-type galaxies. Figure 11 reveals that this diversity is clearly segregated, for log $M_\star$ from 8.4 to 10.4, in terms of stellar mass surface density and Hubble type.

7.3. Radial gradients of the mass-weighted age

In González Delgado et al. (2014b) we presented the results for the inner gradients in (light-weighted) age (and $\Sigma_\star$), and its relation with $M_\star$ for 107 galaxies. The gradient of the light-weighted age was computed in the inner HLR of each galaxy as the difference between the value of $\langle \log \text{age} \rangle_L$ at 1 HLR and the value at the nucleus. In this work, we present the gradients of the mass weighted age $\nabla \langle \log \text{age} \rangle_M$ as a function of both $M_\star$ and $\Sigma_\star$ in our defined bins. Here we follow a different approach for the calculation of the gradients. We perform a robust linear fit over the entire inner 1 HLR. The distribution of the slope of the fit for all galaxies as a function of stellar mass, stellar mass surface density, and Hubble type is shown in Fig. 12. On average, negative gradients are detected for all bins of the three parameters. A clear trend is seen both for $M_\star$ (left panel) and $\Sigma_\star$ (central panel) in the sense that the gradient is steeper (more negative) as the value of the parameter decreases. However, for the mass, the trend breaks in the lowest-mass bin where the average value increases with respect to the previous bin. The range of variation of the value of the gradients is particularly evident, as we have seen in previous plots, for the two lower bins, especially the lowest one, where a few galaxies show positive gradients, thus rising the average value of the distribution. As for the Hubble type (right panel), two break points can be seen. The slope of early-type galaxies are very similar considering the dispersion, with average values of −0.15 dex/HLR for E and −0.10 dex/HLR for Sa galaxies, decreasing to the lowest value for Sc (−0.31 dex/HLR), and then rising again for the Sd bin (−0.23 dex/HLR), which presents the largest dispersion. Some of the Hubble-type bins also show a few positive galaxies as seen in the upper quartile of E, Sd, and particularly Sd galaxies. Again, the range of the interquartile for late-type galaxies (Sc and Sd) is wider than the other bins, which hints to a second dependence on other parameters, as seen in Sect. 7.2. Most of the galaxies that show positive gradients have values compatible with flat or negative slopes taking into account their errors. The other very few cases that show steeper positive gradients are peculiar galaxies with a young star forming region in the center of the galaxy. On average, they do not show a particularly high sSFR value for their mass.

We explore now a possible multivariate dependence of the $\nabla \langle \log \text{age} \rangle_M$ on both $M_\star$ and $\Sigma_\star$. In this case, we perform a linear fit over the inner 1 HLR of the averaged mass-weighted age profiles presented in Fig. 8. The results are summarized in Table 3 and visually represented in Fig. 13. If we look at the values within a particular $\Sigma_\star$ bin (columns), there is not a particular second dependence, within the errors, on the four largest $M_\star$ bins. However, $\Sigma_\star$ shows an important dependence on the low-mass range (8.4–10.4) [log $M_\star$], where the slope becomes steeper (more negative) with increasing mass. This dependence

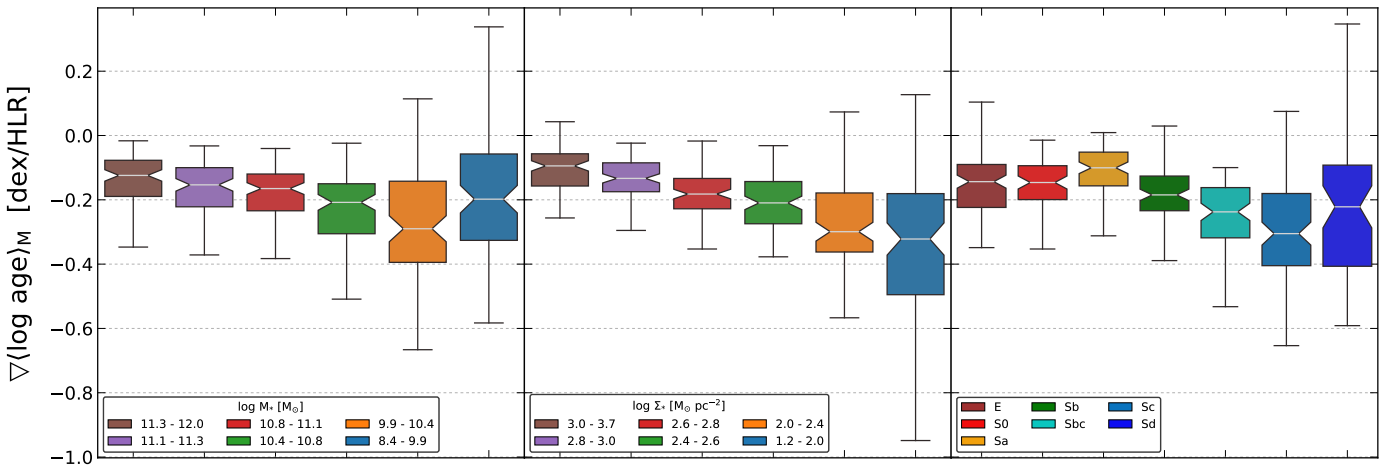

Fig. 12. Box plot diagram of the mass-weighted age gradients $\nabla\langle\log\ \mathrm{age}\rangle_M$ (dex/HLR) over the inner 1 HLR for all galaxies as a function of stellar mass (*left*), stellar mass surface density (*center*), and Hubble type (*right*). The gray horizontal line in each notched box plot shows the median of the distribution.

Table 3. Mass-weighted age gradients $\nabla\langle\log\ \mathrm{age}\rangle_M$ of the inner 1 HLR and inner 1 HMR of the average radial profile of each stellar mass and stellar mass surface density bin.

log M_* [$M_\odot$]	log $\Sigma_\star$[$M_\odot$ pc^{-2}]					
	1.2–2.0	2.0–2.4	2.4–2.6	2.6–2.8	2.8–3.0	3.0–3.7
			$\nabla\langle\log\ \mathrm{age}\rangle_M$ [dex/HLR]			
8.4–9.9	–0.26 ± 0.04	–0.19 ± 0.02	–	–	–	–
9.9–10.4	–0.52 ± 0.03	–0.31 ± 0.02	–0.22 ± 0.03	–	–	–
10.4–10.8	–	–0.36 ± 0.03	–0.21 ± 0.02	–0.20 ± 0.02	–0.15 ± 0.02	–0.11 ± 0.03
10.8–11.1	–	–0.31 ± 0.02	–0.23 ± 0.02	–0.20 ± 0.02	–0.16 ± 0.03	–0.14 ± 0.03
11.1–11.3	–	–	–0.25 ± 0.03	–0.16 ± 0.02	–0.17 ± 0.03	–0.13 ± 0.03
11.3–12.0	–	–	–0.20 ± 0.02	–0.18 ± 0.03	–0.15 ± 0.02	–0.10 ± 0.02
			$\nabla\langle\log\ \mathrm{age}\rangle_M$ [dex/HMR]			
8.4–9.9	–0.19 ± 0.04	–0.15 ± 0.04	–	–	–	–
9.9–10.4	–0.37 ± 0.03	–0.24 ± 0.03	–0.19 ± 0.02	–	–	–
10.4–10.8	–	–0.22 ± 0.02	–0.17 ± 0.02	–0.14 ± 0.02	–0.11 ± 0.02	–0.10 ± 0.04
10.8–11.1	–	–0.24 ± 0.02	–0.17 ± 0.02	–0.14 ± 0.02	–0.12 ± 0.03	–0.12 ± 0.02
11.1–11.3	–	–	–0.17 ± 0.03	–0.11 ± 0.02	–0.15 ± 0.03	–0.09 ± 0.02
11.3–12.0	–	–	–0.14 ± 0.03	–0.14 ± 0.03	–0.12 ± 0.02	–0.09 ± 0.02

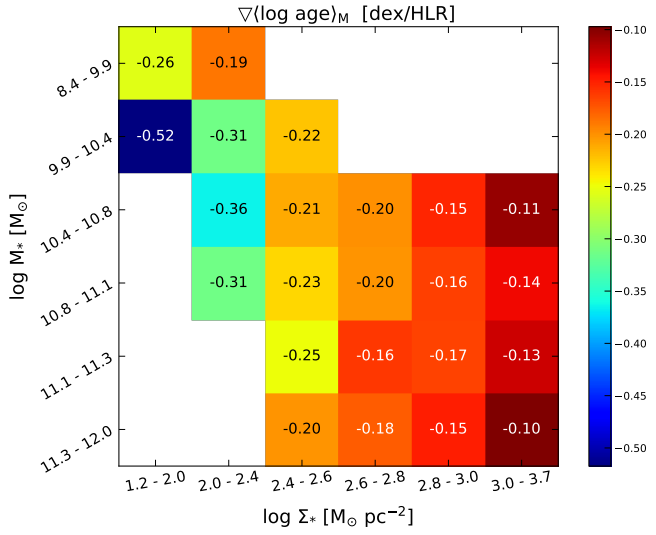

Fig. 13. Visual representation of Table 3 of the mass-weighted age gradients $\nabla\langle\log\ \mathrm{age}\rangle_M$ (dex/HLR) estimated over the inner 1 HLR for all galaxies as a function of both $M_\star$ and $\Sigma_\star$.

disappears and the values of the slope fall into a plateau at the interface of the second and third $M_\star$ bins ($\sim 10^{10.4}$ $M_\odot$). On the other hand, if we inspect the variation of $\nabla\langle\log\ \mathrm{age}\rangle_M$ with $\Sigma_\star$ within a particular $M_\star$ bin (rows), a clear trend is found. The slope flattens (less negative) with increasing values of $\Sigma_\star$. Thus, the wider range of values for the two lowest $M_\star$ and $\Sigma_\star$ bins seen in Fig. 12 can be understood in terms of a stronger dependence on a second parameter in this regime.

As discussed in Sect. 5, stellar mass is more concentrated on average than light. We turn now to the question of whether or not the gradient results hold if the calculations are made based on the mass metric (HMR) instead of a light metric (HLR). Table 3 shows the $\nabla\langle\log\ \mathrm{age}\rangle_M$ in the inner 1 HMR for both $M_\star$ and $\Sigma_\star$ bins. The results are similar to those based on the light metric. On average, galaxies display negative gradients, but these less steep than the light counterpart. Similarly, the trend with parameters $M_\star$ and $\Sigma_\star$ also remains. These results indicate than the inner HLR or HMR gradients depend primarily on $\Sigma_\star$ and to a lesser degree on $M_\star$ for galaxies with $\Sigma_\star > 100$ $M_\odot$ pc^{-2}. As we have seen previously, the value of $\Sigma_\star$ at 1 HLR is an informative representative of the average $\Sigma_\star$ for the whole galaxy. It is also a

characteristic value for the $\Sigma_\star$ of the disk. Low values of $\Sigma_\star$ on the disk, because of the local $\Sigma_\star$ – $\langle \log \text{age} \rangle_L$ relation, present lower values of $\langle \log \text{age} \rangle_L$ (a younger disk), and therefore, larger $\langle \log \text{age} \rangle_M$ gradients. These results can be understood in light of Fig. 5: galaxies in the same $M_\star$ bin display values of t_{80}^{In} but their t_{80}^{Out} decrease with $\Sigma_\star$. This is the result of galaxies forming their disk (or envelope) at a later epoch.

8. Conclusions

In this paper, we studied the mass assembly time scales of 661 galaxies observed by CALIFA using the 3.5 m telescope in Calar Alto. Our sample covers stellar masses from $10^{8.4}$ to 10^{12} $M_\odot$ (for a Salpeter IMF), including ellipticals, S0, and spirals from Sa to Sd. We applied the fossil record method of the stellar populations using the STARLIGHT code and a combination of SSP spectra from González Delgado et al. (2005) plus Vazdekis et al. (2015). This base comprises eight metallicities from log log $Z/Z_\odot$ = −2.28 to +0.40, and 37 ages from 1 Myr to 14 Gyr. With the aid of our PyCASSO pipeline we processed the spectral fitting results to produce 2D ($R \times t$) maps of the mass growth and mass-weighted age, from which we obtain temporal and spatially resolved information. For each galaxy, the $\langle \log \text{age} \rangle_M$ maps are azimuthally averaged to produce radial profiles, both in units of HLR and HMR. All the analyzed quantities are stacked as a function of stellar mass, stellar mass surface density, and Hubble type to explore the main trends.

Our main results are as follows:

1. Spatially resolved mass assembly. On average, galaxies form inside-out at any given stellar mass, stellar mass surface density, and Hubble type bin, including the lowest-mass systems in our mass range. This result concerning low-mass galaxies could not be confirmed in our previous work Pérez et al. (2013).
2. Galaxies show a significant diversity in their characteristic formation epochs for lower-mass systems. This diversity can be understood in terms of a strong dependence of the mass assembly time scales on $\Sigma_\star$ and Hubble type in the lower-mass range ($10^{8.4}$ to $10^{10.4}$), while this dependence is very mild in higher-mass bins.
3. The lowest HMR/HLR ratio is found for galaxies between $10^{10.4}$ and $10^{11.1}$ $M_\odot$, where galaxies are 25% smaller in mass than in light. Low-mass galaxies ($10^{8.4}$–$10^{9.9}$ $M_\odot$) show the largest ratio with HMR/HLR ∼ 0.89. Sb and Sbc galaxies present the lowest HMR/HLR ratio (0.74). This results supports the result that galaxies grow inside-out.
4. At $z = 1$, the downsizing pattern is, on average, spatially preserved. The inner parts of the most massive galaxies attained almost all their final mass (∼97%) and the envelopes were in the last stages of their assembly (∼85%). On the other hand, the inner parts of low-mass galaxies were at ∼70%, while the outer parts close to half of their final value (∼56%).
5. We found, on average, negative $\langle \log \text{age} \rangle_M$ gradients in the inner 1 HLR (or HMR) for all galaxies. The radial profile flattens (slope less negative) with increasing values of $\Sigma_\star$. There is no significant dependence on $M_\star$ within a particular $\Sigma_\star$ bin, except for the lowest bin ($10^{8.4}$–$10^{9.9}$ $M_\odot$), where the gradients become steeper.

In summary, thanks to the large FoV of PPAK which covers galaxies in their entire optical extent, CALIFA has proven to be an excellent benchmark, in combination with the fossil record method, to test the formation and evolution of galaxies in terms of their spatially resolved properties. We have shown a complex multivariate dependence on stellar mass, stellar mass surface density, and Hubble type of the mass assembly time scales and mass-weighted age gradients which once again demonstrates the convenience of these parameters in organizing the spatially resolved properties of galaxies.

Acknowledgements. CALIFA is the first legacy survey carried out at Calar Alto. The CALIFA collaboration would like to thank the IAA-CSIC and MPIA-MPG as major partners of the observatory, and CAHA itself, for the unique access to telescope time and support in manpower and infrastructures. We also thank the CAHA staff for their dedication to this project. We are grateful for the support of the IAA Computing group. Support from the Spanish Ministerio de Economía y Competitividad, through projects AYA2016-77846-P, AYA2014-57490-P, AYA2010-15081, and Junta de Andalucía P12-FQM-2828. R.C.F. acknowledges support from CNPq and FAPESC. S.F.S. thanks PAPIIT-DGAPA-IA101217 project and CONACYT-IA-180125. This research made use of Python (http://www.python.org); Numpy (Van Der Walt et al. 2011), Astropy (Astropy Collaboration et al. 2013), Pandas (McKinney 2011), Matplotlib (Hunter 2007), and Seaborn (Waskom et al. 2016). We thank the referee for very useful comments that improved the presentation of the paper.

References

Abazajian, K. N., Adelman-McCarthy, J. K., Agüeros, M. A., et al. 2009, ApJS, 182, 543
Astropy Collaboration, Robitaille, T. P., Tollerud, E. J., et al. 2013, A&A, 558, A33
Athanassoula, E., Rodionov, S. A., Peschken, N., & Lambert, J. C. 2016, ApJ, 821, 90
Aumer, M., & White, S. D. M. 2013, MNRAS, 428, 1055
Aumer, M., White, S. D. M., & Naab, T. 2014, MNRAS, 441, 3679
Avila-Reese, V., & Firmani, C. 2000, Rev. Mex. Astron. Astrofis., 36, 23
Baugh, C. M., Cole, S., & Frenk, C. S. 1996, MNRAS, 283, 1361
Birnboim, Y., Dekel, A., & Neistein, E. 2007, MNRAS, 380, 339
Brook, C. B., Kawata, D., Martel, H., Gibson, B. K., & Bailin, J. 2006, ApJ, 639, 126
Brook, C. B., Stinson, G. S., Gibson, B. K., et al. 2012, MNRAS, 426, 690
Buitrago, F., Trujillo, I., Conselice, C. J., et al. 2008, ApJ, 687, L61
Bundy, K., Bershady, M. A., Law, D. R., et al. 2015, ApJ, 798, 7
Cappellari, M., & Copin, Y. 2003, MNRAS, 342, 345
Cardelli, J. A., Clayton, G. C., & Mathis, J. S. 1989, ApJ, 345, 245
Cid Fernandes, R., Mateus, A., Sodré, L., Stasińska, G., & Gomes, J. M. 2005, MNRAS, 358, 363
Cid Fernandes, R., Pérez, E., García Benito, R., et al. 2013, A&A, 557, A86
Cid Fernandes, R., González Delgado, R. M., García Benito, R., et al. 2014, A&A, 561, A130
Croton, D. J., Springel, V., White, S. D. M., et al. 2006, MNRAS, 365, 11
Dekel, A., Birnboim, Y., Engel, G., et al. 2009, Nature, 457, 451
Di Matteo, P., Haywood, M., Gómez, A., et al. 2014, A&A, 567, A122
Dutton, A. A., van den Bosch, F. C., & Dekel, A. 2010, MNRAS, 405, 1690
Elmegreen, D. M., Elmegreen, B. G., Ravindranath, S., & Coe, D. A. 2007, ApJ, 658, 763
Elmegreen, B. G., Bournaud, F., & Elmegreen, D. M. 2008, ApJ, 688, 67
Fisher, D. B., & Drory, N. 2010, ApJ, 716, 942
Fontanot, F., De Lucia, G., Monaco, P., Somerville, R. S., & Santini, P. 2009, MNRAS, 397, 1776
Förster Schreiber, N. M., Shapley, A. E., Erb, D. K., et al. 2011, ApJ, 731, 65
García-Benito, R., Zibetti, S., Sánchez, S. F., et al. 2015, A&A, 576, A135
Genzel, R., Burkert, A., Bouché, N., et al. 2008, ApJ, 687, 59
Genzel, R., Förster Schreiber, N. M., Lang, P., et al. 2014, ApJ, 785, 75
Gil de Paz, A., Madore, B. F., Boissier, S., et al. 2005, ApJ, 627, L29
Gil de Paz, A., Boissier, S., Madore, B. F., et al. 2007, ApJS, 173, 185
Goddard, D., Thomas, D., Maraston, C., et al. 2017, MNRAS, 466, 4731
González Delgado, R. M., Cerviño, M., Martins, L. P., Leitherer, C., & Hauschildt, P. H. 2005, MNRAS, 357, 945
González Delgado, R. M., Cid Fernandes, R., García-Benito, R., et al. 2014a, ApJ, 791, L16
González Delgado, R. M., Pérez, E., Cid Fernandes, R., et al. 2014b, A&A, 562, A47
González Delgado, R. M., García-Benito, R., Pérez, E., et al. 2015, A&A, 581, A103
González Delgado, R. M., Cid Fernandes, R., Pérez, E., et al. 2016, A&A, 590, A44
González Delgado, R. M., et al. 2017, A&A, submitted

Haywood, M., Di Matteo, P., Lehnert, M. D., Katz, D., & Gómez, A. 2013, A&A, 560, A109
Haywood, M., Di Matteo, P., Snaith, O., & Lehnert, M. D. 2015, A&A, 579, A5
Hilz, M., Naab, T., & Ostriker, J. P. 2013, MNRAS, 429, 2924
Hopkins, P. F., Cox, T. J., Younger, J. D., & Hernquist, L. 2009, ApJ, 691, 1168
Hunter, J. D. 2007, Comp. Sci. Eng., 9, 90
Ibarra-Medel, H. J., Sánchez, S. F., Avila-Reese, V., et al. 2016, MNRAS, 463, 2799
Kelz, A., Verheijen, M. A. W., Roth, M. M., et al. 2006, PASP, 118, 129
Larson, R. B. 1976, MNRAS, 176, 31
Lilly, S. J., Carollo, C. M., Pipino, A., Renzini, A., & Peng, Y. 2013, ApJ, 772, 119
Marino, R. A., Gil de Paz, A., Sánchez, S. F., et al. 2016, A&A, 585, A47
Martig, M., Bournaud, F., Teyssier, R., & Dekel, A. 2009, ApJ, 707, 250
Martin, D. C., Fanson, J., Schiminovich, D., et al. 2005, ApJ, 619, L1
McKinney, W. 2011, pandas: powerful Python data analysis toolkit
Mo, H. J., Mao, S., & White, S. D. M. 1998, MNRAS, 295, 319
Muñoz-Mateos, J. C., Gil de Paz, A., Boissier, S., et al. 2007, ApJ, 658, 1006
Naab, T., Johansson, P. H., & Ostriker, J. P. 2009, ApJ, 699, L178
Neistein, E., van den Bosch, F. C., & Dekel, A. 2006, MNRAS, 372, 933
Nelson, E. J., van Dokkum, P. G., Brammer, G., et al. 2012, ApJ, 747, L28
Nelson, E. J., van Dokkum, P. G., Förster Schreiber, N. M., et al. 2016, ApJ, 828, 27
Oser, L., Ostriker, J. P., Naab, T., Johansson, P. H., & Burkert, A. 2010, ApJ, 725, 2312
Patel, S. G., van Dokkum, P. G., Franx, M., et al. 2013, ApJ, 766, 15
Pérez, E., Cid Fernandes, R., González Delgado, R. M., et al. 2013, ApJ, 764, L1
Pezzulli, G., Fraternali, F., Boissier, S., & Muñoz-Mateos, J. C. 2015, MNRAS, 451, 2324
Pilkington, K., Few, C. G., Gibson, B. K., et al. 2012, A&A, 540, A56
Roth, M. M., Kelz, A., Fechner, T., et al. 2005, PASP, 117, 620
Sánchez, S. F., Kennicutt, R. C., Gil de Paz, A., et al. 2012a, A&A, 538, A8
Sánchez, S. F., Rosales-Ortega, F. F., Marino, R. A., et al. 2012b, A&A, 546, A2
Sánchez, S. F., Rosales-Ortega, F. F., Iglesias-Páramo, J., et al. 2014, A&A, 563, A49
Sánchez, S. F., García-Benito, R., Zibetti, S., et al. 2016, A&A, 594, A36
Sánchez-Blázquez, P., Rosales-Ortega, F. F., Méndez-Abreu, J., et al. 2014, A&A, 570, A6
Sánchez-Menguiano, L., Sánchez, S. F., Pérez, I., et al. 2016, A&A, 587, A70
Springel, V., & Hernquist, L. 2005, ApJ, 622, L9
Steinmetz, M., & Navarro, J. F. 2002, New Astron., 7, 155
Szomoru, D., Franx, M., van Dokkum, P. G., et al. 2010, ApJ, 714, L244
Szomoru, D., Franx, M., & van Dokkum, P. G. 2012, ApJ, 749, 121
Szomoru, D., Franx, M., van Dokkum, P. G., et al. 2013, ApJ, 763, 73
Tinsley, B. M. 1968, ApJ, 151, 547
Toomre, A., & Toomre, J. 1972, ApJ, 178, 623
Trujillo, I., Förster Schreiber, N. M., Rudnick, G., et al. 2006, ApJ, 650, 18
Van Der Walt, S., Colbert, S. C., & Varoquaux, G. 2011, Comp. Sci. Eng., 13, 22
van Dokkum, P. G., Whitaker, K. E., Brammer, G., et al. 2010, ApJ, 709, 1018
van Dokkum, P. G., Leja, J., Nelson, E. J., et al. 2013, ApJ, 771, L35
Vazdekis, A., Coelho, P., Cassisi, S., et al. 2015, MNRAS, 449, 1177
Verheijen, M. A. W., Bershady, M. A., Andersen, D. R., et al. 2004, Astron. Nachr., 325, 151
Walcher, C. J., Wisotzki, L., Bekeraité, S., et al. 2014, A&A, 569, A1 (W14)
Waskom, M., Botvinnik, O., Drewokane, et al. 2016, seaborn: v0.7.0 (January 2016)
Wilkinson, D. M., Maraston, C., Thomas, D., et al. 2015, MNRAS, 449, 328
Wuyts, S., Förster Schreiber, N. M., Nelson, E. J., et al. 2013, ApJ, 779, 135
Zheng, Z., Wang, H., Ge, J., et al. 2017, MNRAS, 465, 4572